

**Evidence of electronic structural change at the metal-insulator transition in the perovskite NaOsO<sub>3</sub>**J.-S. Zhou<sup>1,\*</sup>, X.-Y. Li<sup>1</sup> and M. D. Johannes<sup>2</sup><sup>1</sup>*Materials Science and Engineering Program, Mechanical Engineering, University of Texas at Austin, Austin, Texas 78712, USA*<sup>2</sup>*Center for Computational Materials Science, Naval Research Laboratory, Washington D.C. 20375, USA*

(Received 31 August 2023; revised 11 October 2023; accepted 24 October 2023; published 8 November 2023)

NaOsO<sub>3</sub> exhibits an unusual metal-insulator transition (MIT) that has been touted as Slater type, though there are observations that do not entirely conform to this typing. Consistent with a Slater transition, the cell volume and crystal symmetry show no change on cooling through the transition, but both *a* and *b* axes in this *Pbnm* orthorhombic perovskite show a clear kink, and the splitting between them enlarges slightly. Since atomic positions, determined by fitting the intensity of state-of-the-art neutron diffraction data, exhibit no anomalies within the measurement uncertainty, the origin of the *a*-*b* splitting and the kink in the data have not yet been elucidated. Understanding the origin of these subtle structural changes across the transition temperature may provide understanding about the electronic behavior. In this paper, we connect local structural changes to changes in the lattice parameters through (1) well-established structural modeling and (2) density functional theory (DFT) calculations. This approach successfully reveals a subtle but significant change of the O-Os-O bond angle on cooling through  $T_{\text{MIT}}$ . A Madelung energy calculation suggests that this bond angle change signals electron localization in the  $t_{2g}$  orbital complex, and this is verified by DFT, which shows an electronic transition from itinerant to localized electronic behavior along with the bond angle shift. In this detailed structural study, we add an important though heretofore overlooked element in the microscopic picture of the MIT in NaOsO<sub>3</sub>.

DOI: [10.1103/PhysRevB.108.195115](https://doi.org/10.1103/PhysRevB.108.195115)**I. INTRODUCTION**

NaOsO<sub>3</sub> undergoes a sharp metal-insulator transition (MIT) at  $T_{\text{MIT}} = 410$  K [1], accompanied by a long-range colinear G-type antiferromagnetic (AFM) ordering with a moment of  $\sim 1.0 \mu_{\text{B}}$  on Os<sup>5+</sup>, as measured by neutron diffraction [2]. Above the transition temperature, NaOsO<sub>3</sub> is a metal with resistivity at the level of  $10^{-4} \Omega \text{ cm}$  and a weak temperature dependence. Fitting the magnetic susceptibility  $\chi(T)$  to a Curie-Weiss law gives rise to  $\mu_{\text{eff}} = 2.7 \mu_{\text{B}}$ , nearly three times the observed moment in the magnetically ordered phase below  $T_{\text{MIT}}$ , and an unphysically large Weiss constant  $\Theta = -1949$  K. On cooling through  $T_{\text{MIT}}$ , the magnetization jumps in the same way as in other AFMs with canted spins [3,4], and the resistivity has a sharp jump followed by an increase of  $> 10^7$  orders of magnitude as cooling continues to the lowest temperature. Although tremendous efforts have been made, a sound understanding of this seemingly simple transition remains elusive.

As indicated by high-resolution neutron diffraction [2], there are no changes in the structural symmetry or cell volume upon crossing the transition temperature, with the observed jump in resistivity apparently related only to the AFM spin ordering. The combination of chemical sensitivity of absorption and the atomic position sensitivity of diffraction offered by resonant inelastic x-ray scattering (RIXS) can accurately determine electron density in OsO<sub>6</sub> octahedra in both the insulating and metallic states of NaOsO<sub>3</sub>. Consistent with

the neutron diffraction study, the RIXS study [5] also shows no symmetry change from the isosurface of the *5d* electron density of Os ions upon crossing  $T_{\text{MIT}}$ . These observations together with a smaller magnetic moment than that expected from localized  $t_{2g}^3$  electrons on Os<sup>5+</sup> have led authors to the conclusion that the MIT in NaOsO<sub>3</sub> is a case of the rare Slater MIT where a gap at the Fermi energy opens as electrons are scattered differently at the two sublattices of the AFM ordered magnetic structure [6]. An infrared (IR) spectroscopy study [7] indeed revealed the formation of a gap  $\Delta(T)$  that can be fit well to the BCS theory below  $T_{\text{MIT}}$ , which implies a band electronic state remains in the insulating state and is consistent with the Slater MIT. However, other RIXS studies [8,9] offer evidence of correlation fluctuations in the metallic phase above  $T_{\text{MIT}}$ , which is clearly incompatible with the mean-field treatment used in the Slater mechanism.

Band structure calculations [10] indicate that the electronic structure near the Fermi energy is dominated by hybridized Os : *5d* and O : *2p* states formed by the  $pd\pi^*(t_{2g})$  with the  $pd\sigma^*(e_g)$  complex gapped away by  $\sim 1$  eV in the experimental structure. The application of a Hubbard *U* in the nonmagnetic or ferromagnetic (FM) state does not lead to a gap opening at the Fermi energy, even for large values of *U*. The addition of a spin-orbit coupling (SOC) term also precipitates a gap opening or affects the atomic or lattice parameters, likely because the orbital angular momentum is quenched for the  $t_{2g}^3$  orbital occupation in NaOsO<sub>3</sub>. Kim *et al.* [11] have shown that SOC is a key parameter in controlling the balance between the on-site Coulomb repulsion *U* and the bandwidth *W*. In this situation, the correct G-type spin ordering, along with an applied *U*, separates the two connected bands as described

\*jszhou@mail.utexas.edu

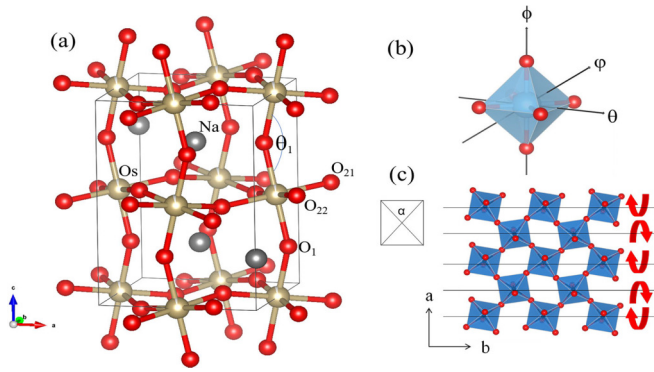


FIG. 1. (a) The structural model of orthorhombic perovskite  $\text{NaOsO}_3$ . (b) An  $\text{OsO}_6$  octahedron with three rotation axes. (c) The perovskite structure with  $\text{OsO}_6$  octahedra projected onto the  $ab$  plane from the  $c$  axis; the rotation around the  $\theta$  axis is indicated by red arrows. The rectangular box standing for exaggerated octahedra illustrates the bond angle  $\alpha < 90^\circ$ .

in a Lifshitz transition. Jung *et al.* [12] have shown that no magnetic ordering of any type can be obtained in the cubic cell within  $\pm 3\%$  variation of the experimental volume. Thus, both octahedral tilting and application of  $U$  are necessary to achieve a full gap at the Fermi energy in the G-type AFM state. The tilting additionally further splits the  $pd\pi$  and  $pd\sigma$  complexes but narrows the bandwidths. With any additional tilting of the octahedra beyond a critical threshold, the moment on  $\text{Os}^{5+}$  drops below the observed value. All these observations are broadly consistent with a Slater transition picture. It should be noted that none of these band models can account for the high Néel transition temperature observed in  $\text{NaOsO}_3$ . While this is readily solved by a calculation based on the Hubbard model [13], there is no experimental evidence to support the characteristically localized electrons of this model in the magnetically ordered state.

In this paper, we revisit density functional theory (DFT) calculations in the context of sensitive neutron diffraction data and structural models, employing both full structural relaxations and electronic structure results to tie an overlooked but important  $\text{O}_{21}\text{-Os-O}_{22}$  bond angle  $\alpha$  (see Fig. 1(c)) to electronic localization. We begin by noting that, although the symmetry and volume do not change across the transition, the  $a$  and  $b$  lattice parameters change abruptly in opposite directions, preserving the volume. We argue that these changes are explained by a change in the bond angle  $\alpha$  and that  $\alpha$  is established by a balance between a universal structural distortion in the orthorhombic perovskites [14] that shifts the value of  $\alpha$  away from  $90^\circ$  and the preference for  $\alpha = 90^\circ$  for localized electrons in the  $t_{2g}$  orbital. Thus, the transition is characterized by a shift from itinerant to localized paradigms.

## II. EXPERIMENTAL OBSERVATIONS AND CRYSTALLOGRAPHIC MODEL

The  $Pbnm$  structure is the most popular one in the perovskite family  $ABX_3$  and can accommodate rich structural distortions away from cubic, including the tilting and rotation of octahedra, bond length splitting, and angular octahedral distortion. In  $3d$  transition metal perovskites, it has been

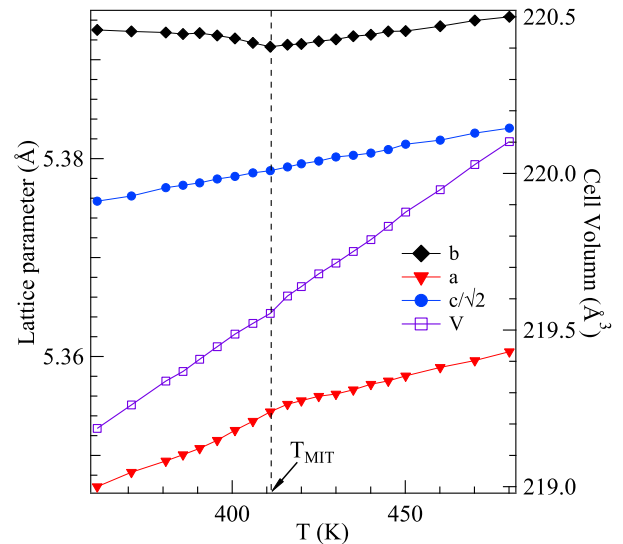


FIG. 2. Temperature dependence of lattice parameters for  $\text{NaOsO}_3$ , data are after Ref. [2]. The error bars are smaller than symbols.

theoretically shown that the MIT is coupled closely to these cooperative elastic fluctuations [15], and a Mott-Hubbard transition has been widely found to be first order with the long-range magnetic ordering sometimes coincident and sometimes following at a lower temperature [16]. A canonical example is the perovskite  $\text{RNiO}_3$  ( $R$  = rare earth) [17–19]. A strong first-order MIT has  $T_N = T_{\text{MIT}}$  for  $R = \text{Pr, Nd}$  and  $T_N < T_{\text{MIT}}$  for the smaller rare earths. The highest occupied electronic states are in the  $pd\sigma^*$  manifold, and the electronic-state change from itinerant to localized behavior is accompanied by a change of the cell volume.

In  $\text{NaOsO}_3$ , no change in atomic positions or electron density are observed upon crossing the MIT within the resolution of a state-of-the-art experiment [2,5]. However, the lattice changes in response to an electronic-state transition are expected to be more subtle for the low-spin  $5d$  electronic state where the wave function is more extended than in  $3d$  or  $4d$  systems. Although atomic positions determined by fitting the peak intensity of neutron diffraction entail considerable uncertainty, the angle-resolved diffraction used for calculating lattice parameters provides much more accuracy (to seven or eight significant figures). This suggests that, by extracting local structure from the lattice parameters through careful structural models, a meaningful correlation can be made between necessarily small local structural changes and any electronic transitions that accompany them. With this construct in mind, we concentrate on a specific subtle change in  $\text{OsO}_6$  octahedra upon crossing  $T_{\text{MIT}}$  via a thorough structural analysis and explicate its relevance for the electronic state in  $\text{NaOsO}_3$ . Whereas the cell volume reported does not show any discernible changes on crossing  $T_{\text{MIT}}$ , the  $a$  and  $b$  axes in the structure with the  $Pbnm$  setting, change dramatically, as shown in Fig. 2. The relevance of these lattice parameter changes at  $T_{\text{MIT}}$  has been largely ignored by both experimental and theoretical groups, and its impact on electronic aspects has not been explored.

The  $Pbnm$  distortion away from the cubic  $Pm-3m$  structure occurs because of the bonding mismatch for the geometric tolerance factor  $t \equiv (A-X)/\sqrt{2}(B-X) < 1$  in a perovskite  $ABX_3$  compound. In oxides, the distortion is a  $GdFeO_3$ -type orthorhombic distortion in which the octahedral tilting system is described by a primary octahedral-site rotation  $\varphi$ , see Fig. 1(b). Lattice parameters can be derived from  $\varphi$  through the formula given by O’Keeffe and Hyde [20]:

$$\begin{aligned} a &= d\sqrt{8} \cos \varphi, \\ b &= d \left[ \frac{8(2 + \cos^2 \varphi)}{3} \right]^{1/2}, \\ c &= d \left( \frac{48}{1 + 2 \sec 2\varphi} \right)^{1/2}, \end{aligned} \quad (1)$$

where  $d$  is the  $B-X$  bond distance. The primary rotation  $\varphi$  can be determined by the atomic positions, for example, from  $X''$  in 8(d) ( $x, y, z$ ) of Wyckoff position, for  $O_{21}$  or  $O_{22}$  in Fig. 1(a):

$$\begin{aligned} x &= \frac{3\sqrt{3} + \tan \varphi}{\sqrt{48}}, \\ y &= \frac{2 - \sqrt{3} \sin \varphi \cos \varphi + \cos^2 \varphi}{8 + 4\cos^2 \varphi}, \\ z &= -\frac{\tan \varphi}{\sqrt{48}}. \end{aligned} \quad (2)$$

To have a clear vision of the relationship between the octahedral-site rotation and lattice parameters, the primary rotation can be decomposed into two rotations around the 110 and 001 axes of the primary cell or by the same decomposition locally in an octahedron, as indicated by  $\theta$  and  $\phi$  in Fig. 1(b). The rotation around  $\phi$  (or 001) can change the overall dimension of the  $ab$  plane but not the relationship between  $a$  and  $b$ . As shown in Fig. 1(c), however, the rotation around  $\theta$ , which is related to  $\theta_1$  in the overall crystal structure by  $2\theta = 180 - \theta_1$ , enhances the buckling in the  $ab$  plane along the  $a$  axis and leads to  $b > c/\sqrt{2} > a$ . If rigid octahedra are assumed, a simulation using the software SPuDs [21] indicates that the relation  $b > c/\sqrt{2} > a$  holds for all values of this rotation, yielding a smooth transition to the cubic structure. However, a crossover from  $b > a$  to  $b < a$  can be found in orthorhombic perovskite oxide systems as the  $t$  factor approaches 1 from  $t < 1$  [22]. This apparent lattice parameter anomaly can be well explained by abandoning the rigid octahedra assumption and considering a specific octahedral-site distortion: a slight reduction from  $90^\circ$  in the  $O_{21}$ -Os- $O_{22}$  bond angle  $\alpha$  (open to the  $a$  axis), as shown in Fig. 1(c). In this scenario, the reduction of the  $a$  axis due to the  $\theta$  rotation is compensated by the now elongated octahedra along the  $a$  axis, which simultaneously reduces the  $b$  axis; the combination of these two changes eventually makes  $a > b$ . In summary, the behavior of  $b-a$  is controlled by both the octahedral-site distortion and the octahedral-site rotation in a  $Pbnm$  perovskite.

Returning to the temperature dependence of lattice parameters of  $NaOsO_3$  in Fig. 2, the difference  $b-a$  increases significantly on cooling through  $T_{MIT}$ . The question is whether the pronounced change of lattice parameters is due to a rigid

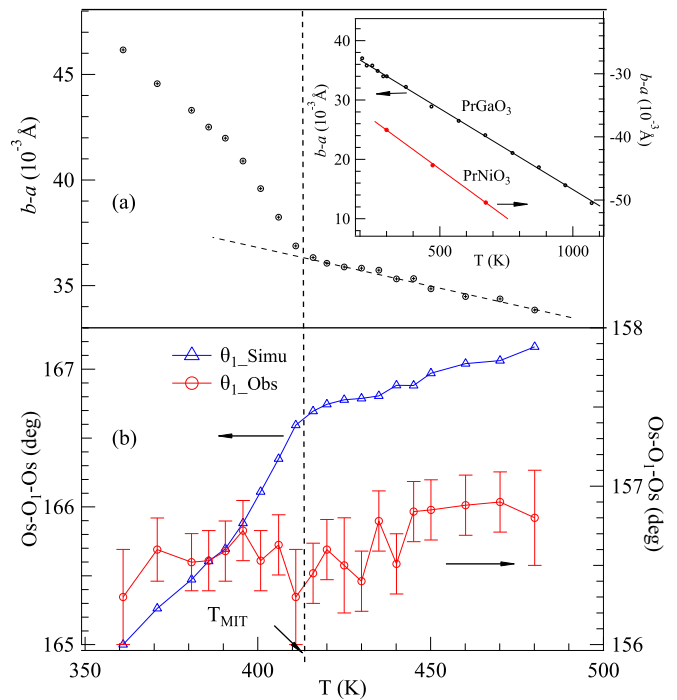


FIG. 3. Temperature dependencies of (a) the difference of lattice parameters,  $b-a$ , of  $NaOsO_3$  and  $PrGaO_3$  and  $PrNiO_3$  in the insert; (b) the simulated and the observed bond angle  $Os-O_1-Os$  in  $NaOsO_3$ .

octahedral change in the  $\theta$  rotation or to an octahedral-site distortion as measured by the angle  $\alpha$  or both. These two angles can be obtained directly from the refinement of neutron diffraction. Unfortunately, no clear changes of either of these two parameters can be discerned beyond the measurement uncertainty.

By taking advantage of the very high precision of the measured lattice parameters, the relative change of the octahedral rotation angle  $\theta_1$  in Fig. 1(a) on crossing  $T_{MIT}$  can be extracted through the formula  $\sin(\theta_1/2) \approx a/b$  if the octahedral-site rotation is the sole source for the change of lattice parameters, i.e., there is no octahedral distortion. Figure 3 displays the temperature dependencies of  $b-a$ , the directly measured value of  $\theta_1$  from neutron data, and the simulated rotation angle  $\theta_1$  derived from the lattice parameters. Corresponding to an abrupt increase of  $b-a$  on cooling through  $T_{MIT}$ , the simulated  $\theta_1$  drops, indicating more buckled  $ab$  planes. Here,  $\theta_1$  from the refinement of neutron diffraction differs from the simulated one by  $\Delta\theta = 10^\circ$ , signaling that  $\sin(\theta_1/2) \approx a/b$  is oversimplified. However, the most important message is that the relative change of  $\theta_1$  required to account for the change of  $b-a$  on cooling through  $T_{MIT}$  is clearly larger than the measurement uncertainty [the size of error bars in Fig. 3(b)] of neutron diffraction. The absence of any change in the observed  $\theta_1$  on cooling through  $T_{MIT}$  implies that the local structural change measured by the angle  $\alpha$  takes place at the transition.

Following the same protocol, we can simulate the primary rotation  $\varphi$  shown in Fig. 1(b) based on the lattice parameters in a formula given by O’Keeffe and Hyde [20]:

$$\varphi = \cos^{-1} \left( \frac{\sqrt{2}a^2}{bc} \right), \quad (3)$$

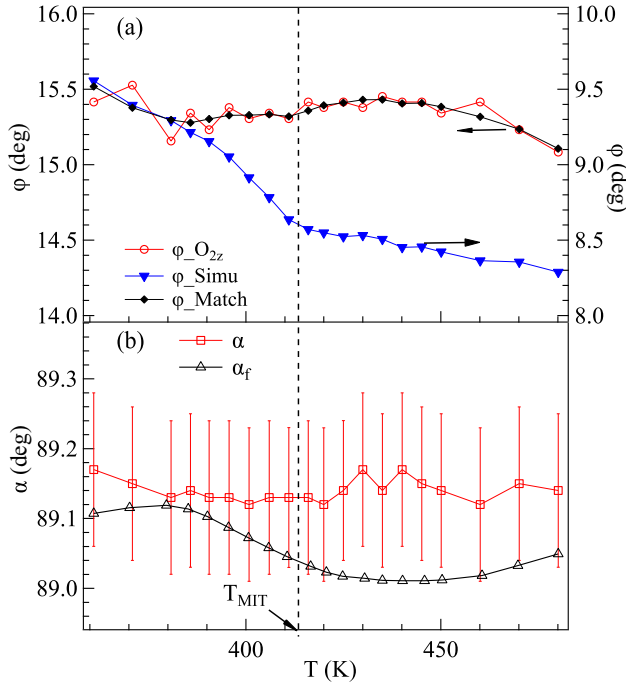


FIG. 4. Temperature dependencies of (a) the primary rotation  $\varphi$ ; (b) the  $O_{21}$ -Os- $O_{22}$  bond angle  $\alpha$ .

again assuming the octahedra are perfectly regular. Figure 4(a) displays the simulated primary rotation  $\varphi_{\text{simu}}$  as derived from the measured lattice parameters and the primary rotation calculated from the oxygen position determined by neutron diffraction through Eq. (2), which is denoted as  $\varphi_{O_{2z}}$ . Again, the absolute difference between the two temperature dependencies of  $\varphi(T)$  implies the octahedra are not perfectly regular. An obvious local distortion is that the angle  $\alpha$  in Fig. 1(c) deviates from  $90^\circ$ . Woodward *et al.* [23] have described the lattice parameter correction caused by this local distortion in the relationship:

$$\frac{b}{b_u} = \sqrt{2} \sin \alpha, \quad \frac{a}{a_u} = \sqrt{2} \cos \alpha, \quad (4)$$

where  $a_u$  and  $b_u$  are for a cell with  $\alpha = 90^\circ$ . We enter  $a_u$  and  $b_u$  of Eq. (4) into Eq. (3) and use  $\alpha$  as a fitting parameter to make the  $\varphi_{\text{simu}}$  match with the observed  $\varphi_{O_{2z}}$ . The results of forced matching between the two  $\varphi(T)$ 's is shown along with  $\varphi_{\text{simu}}$  and  $\varphi_{O_{2z}}$  in Fig. 4(a). The corresponding fitting parameter  $\alpha_f(T)$  is displayed in Fig. 4(b) with the measured values of  $\alpha(T)$ . It is quite remarkable that the difference between  $\alpha_f(T)$  and  $\alpha(T)$  from neutron diffraction is within  $0.15^\circ$ . It implies that the site distortion  $\alpha$  is a dominant octahedral-site distortion in  $\text{NaOsO}_3$ . The measurement uncertainty of the observed  $\alpha(T)$  is too large to distinguish any change of  $\alpha(T)$  at  $T_{\text{MIT}}$ . In contrast, the error bars for  $\alpha_f(T)$  are smaller than the symbol size in the plot. The temperature dependence of  $\alpha_f$  is significant and is the main result of this paper;  $\alpha_f$  appears to increase on cooling through  $T_{\text{MIT}}$ . The remaining question is whether the temperature dependence of  $\alpha_f$  conveys any important message regarding an electronic structure change at  $T_{\text{MIT}}$ .

### III. CORRELATION OF LOCAL STRUCTURAL DISTORTION AND THE ORBITAL OCCUPATION

Before elaborating on the meaning of the change in  $a_f$  at  $T_{\text{MIT}}$ , it is useful to discuss octahedral-site distortions as compared with rigid rotations in perovskites. Here,  $\alpha < 90^\circ$  is commonly found in the  $Pbnm$  perovskite oxides where the octahedral-site tilting angles are relatively small and the  $t$  factor is  $\sim 1$  [22]. In the  $R\text{FeO}_3$  family, for example,  $\alpha$  starts to deviate from  $90^\circ$  for rare-earth ions with an ionic radius larger than that of Gd. A progressive decrease of  $\alpha$  continues as the ionic radius further increases in the family; the total change of  $\alpha$  from  $R = \text{Gd}$  to  $\text{La}$  is  $< 1^\circ$  [22]. The decrease of  $b-a$  from  $\text{GdFeO}_3$  to  $\text{LaFeO}_3$  results from a combination of the reduced octahedral-site rotation and the reduced angle  $\alpha$ . The reduced octahedral-site rotation can explain a decrease of  $b-a$  as the  $t$  factor increases toward 1, but the change of rotation alone cannot account for  $b-a < 0$  in the orthorhombic structure with rigid octahedra. For the perovskite families with the  $t$  factor approaching 1, such as in the series  $\text{RGaO}_3$ ,  $\text{RCoO}_3$ , and  $\text{RNiO}_3$ ,  $b-a < 0$  indeed occurs, which directly illustrates the consequence of the octahedral-site distortion [22]. This intrinsic local distortion is in line with the theorem that “perfect regularity of the octahedra is incompatible with fixed rotation axes” [20]. For  $\text{NaOsO}_3$ ,  $t = 0.9989$  is obtained by using SPuDs where the tabulated ionic radii of  $\text{Na}^+$ ,  $\text{Os}^{5+}$ , and  $\text{O}^{2-}$  are used. Like other orthorhombic perovskites with  $t$  factor close to 1, a value of  $\alpha_f(T) < 90^\circ$  for  $\text{NaOsO}_3$  for  $360 < T < 490$  K is expected. To provide context for discussing whether an increase in  $\alpha$  at the MIT indicates a change of electronic structure, it is useful to examine other perovskite insulators over a wide range of temperature.  $\text{PrGaO}_3$ , which is a diamagnetic (from the Ga-O array) insulator and has been thoroughly studied by x-ray diffraction from 12 to 1200 K [24], and  $\text{PrNiO}_3$  [25], which is metallic, are nice examples. We again turn to the change of lattice parameters of these two perovskites. A detailed comparison of  $b-a$  for  $\text{NaOsO}_3$  is given in Fig. 3(a), and the same quantity for  $\text{PrGaO}_3$  and  $\text{PrNiO}_3$  is given in the insert. The linear increase of  $b-a$  as temperature decreases in insulating  $\text{PrGaO}_3$  is comparable with that of  $\text{NaOsO}_3$  at  $T > T_{\text{MIT}}$ . In the metallic  $\text{PrNiO}_3$ ,  $b-a$  becomes negative and changes linearly as temperature decreases. A negative  $b-a$  is indicative of an even larger octahedral-site distortion in metallic  $\text{PrNiO}_3$  than that in the metallic phase of  $\text{NaOsO}_3$ ;  $\alpha$  is  $88.5^\circ$  at 300 K and reduced to  $88.2^\circ$  at 670 K in  $\text{PrNiO}_3$ . Interestingly, the slopes of fitting lines to the three sets of  $b-a$  (the data above  $T_{\text{MIT}}$  in  $\text{NaOsO}_3$ ) in these perovskites are very close; it is  $-3.8 \times 10^{-5} \text{ \AA/K}$  for  $\text{NaOsO}_3$ ,  $-3.1 \times 10^{-5} \text{ \AA/K}$  for  $\text{PrNiO}_3$ , and  $-2.7 \times 10^{-5} \text{ \AA/K}$  for  $\text{PrGaO}_3$ . An abrupt change of  $b-a$  on crossing  $T_{\text{MIT}}$  in  $\text{NaOsO}_3$  then must reflect a change of electronic behavior as intrinsic structural distortions give rise to a smooth increase of  $b-a$  on cooling if the electronic phase is constant.

Octahedral-site distortions in many cases reflect the orbital occupation. A typical example is the cooperative Jahn-Teller (JT) distortion as seen in  $\text{LaMnO}_3$ , where the electron occupation of the  $3y^2-r^2$  and  $3x^2-r^2$  orbitals alternating in the lattice array of  $ab$  plane makes a distorted octahedral site with two long and four short bonds [14]. However, it has rarely been studied whether orbital occupation could change the

bond angles in octahedra in the orthorhombic perovskites. In  $\text{NaOsO}_3$ , itinerant electrons in the  $\pi^*$  band do not prefer any local bonding configuration.  $\text{NaOsO}_3$  in the metallic phase above the transition adopts a crystal structure with intrinsic distortions like other orthorhombic perovskites, i.e.,  $\alpha < 90^\circ$ . However, localized electrons in  $t_{2g}$  orbitals would prefer a normal  $\text{O}_{21}\text{-Os-O}_{22}$ , i.e.,  $\alpha = 90^\circ$  and a normal  $\text{O}_1\text{-Os-O}_2$  bond angle. Therefore, any transition from itinerant electrons to localized electrons on cooling through  $T_{\text{MIT}}$  would create a competing force against the intrinsic octahedral-site distortion. Since the connection between the lattice parameter difference  $b-a$  and the octahedral-site distortion described by  $\alpha$  is well justified in the description above, we will consider the change of lattice parameters  $b-a$  instead of  $\alpha$  (it is difficult to determine  $\alpha$  precisely in a structural study) and its connection to the orbital occupation in some well-known systems. In the case of  $\sigma^*$  band electrons, the orbital ordering for the  $e_g$  electrons creates a bond-length distortion as well as the site preference for  $\alpha = 90^\circ$ . The manganite  $\text{La}_{1-x}\text{Sr}_x\text{MnO}_3$  has the same structure as  $\text{NaOsO}_3$ . Hole doping induces an evolution from an A-type AFM insulator to a FM metal. The coincident rapid shrinkage of  $b-a$  serves as a good indicator of how  $\alpha$  deviates from  $90^\circ$ . Hole doping in the system reduces  $b-a$  due to the combination of a decreased octahedral-site rotation and  $\alpha$  deviating from  $90^\circ$ . However,  $b-a < 0$  is not allowed in the  $Pbnm$  structure with rotating rigid octahedra only. The cooperative JT bond distortion associated with  $\text{Mn}^{3+}$  in  $\text{La}_{1-x}\text{Sr}_x\text{MnO}_3$  can influence the magnitude of  $b-a$ , but it maintains a positive value. The observation of  $b < a$  at some point of doping in the  $Pbnm$   $\text{La}_{1-x}\text{Sr}_x\text{MnO}_3$  reflects the deviation of  $\alpha$  from  $90^\circ$ . An abrupt drop of  $b-a$  on passing a critical doping  $x = 0.11$  that separates the insulator and metallic phases in the system clearly indicates that electron localization in the  $e_g$  orbital in the insulator phase prefers an  $\alpha$  close to  $90^\circ$  [26]. The stunningly similar behavior of  $b-a$  between the temperature-induced change in  $\text{NaOsO}_3$  and the doping-induced change in  $\text{La}_{1-x}\text{Sr}_x\text{MnO}_3$  suggests that electron localization occurs upon crossing  $T_{\text{MIT}}$  in  $\text{NaOsO}_3$ .

#### IV. MADELUNG ENERGY

To justify the relationship between the orbital occupation and the change of local structural distortion due to Coulomb interaction, we have calculated the Madelung energy in a point-charge model of the basal plane in an  $\text{OsO}_6$  octahedron with an occupied  $xy$  orbital in Fig. 5. The result clearly shows that the Madelung energy minimizes at  $\alpha = 90^\circ$ ; it is clearly a driving force to compete with the intrinsic octahedral-site distortion with  $\alpha < 90^\circ$ . However, the angle dependence of the Madelung energy is extremely small; the difference is on the fourth decimal place. A more quantitative simulation of how a change of electronic behavior can influence the local structure is illustrated by the DFT calculations below, which includes the effects of Os-O hybridization and spin-orbit coupling missed in the point charge model.

#### V. DFT CALCULATION

##### A. Methods

All DFT calculations were performed with VASP [27] using the projector augmented-wave formulation [28] and the PBE

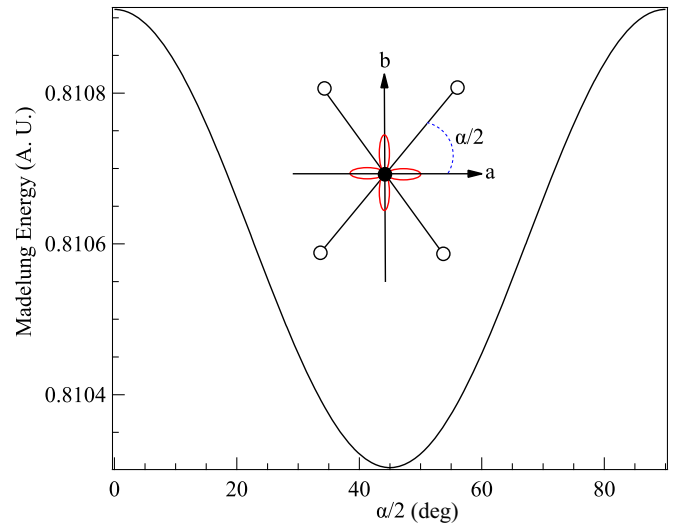


FIG. 5. The Madelung energy in the  $ab$  plane of  $\text{OsO}_4$  as a function of  $\alpha/2$ .

approximation to the exchange correlation functional [29]. To simulate localization, we applied several values of the Hubbard  $U$  parameter to the Os  $5d$  orbitals using the rotationally invariant method of DFT +  $U$  [30]. For each value of  $U$ , we fully relaxed the structure, lattice constants, and atomic positions, within the  $Pbnm$  space group. We used a dense  $k$ -point mesh of  $12 \times 9 \times 12$  and an energy cutoff of 500 eV. For the calculations with SOC, we used the non-collinear version of the VASP code, which treats the SOC with the second variational approach. For all cases, we established the spin-quantization axis along the  $a$  axis, which is experimentally known to be the easy axis. Attempts to establish a different easy axis were unsuccessful, as the self-consistent result always ended up along the  $a$  axis.

##### B. Results

We used DFT to examine how SOC and varying values of localization (as manipulated by increasing  $U$ ; see methods) affect the structure and electronic structure of  $\text{NaOsO}_3$ . We monitor both the gap opening at  $E_F$  via introduction of SOC and  $U$  but also track the subtle changes of crystal structure on crossing the MIT by fully relaxing both the lattice and atomic positions for each different  $U$ . We begin our calculation starting with the nonmagnetic state without SOC (State 1) and the nonmagnetic state with SOC (State 2). The electronic structure and density of states (DOS) obtained is like others reported in the literature [10–12]. Imposing the G-type AFM spin order along with SOC but without any correction to the generalized gradient approximation (GGA) exchange correlation function (State 3) results in a deep pseudogap at  $E_F$ . This gap progressively widens to a true gap as the value of  $U$  is increased from 1 eV (State 4) to 2 eV (State 5). The evolution of the DOS through the various described conditions is shown in Fig. 6.

An analysis of the character of electronics states for  $U = 2.0$  eV with imposed G-type AFM ordering is shown in Fig. 7. In this  $5d$  transition-metal oxide, the exchange energy is

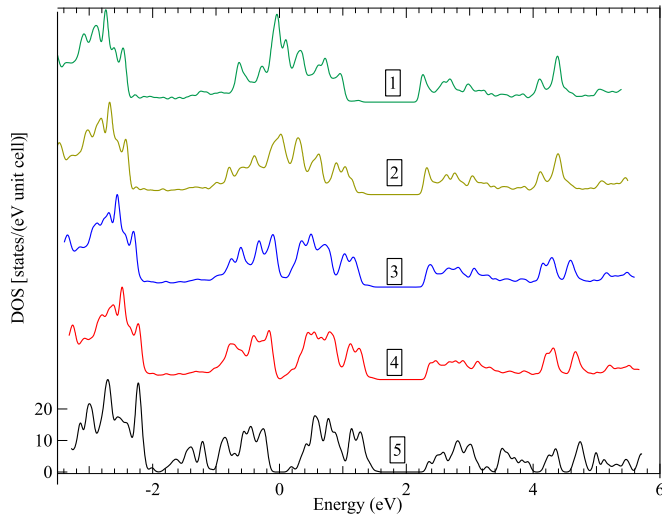


FIG. 6. The density of states (DOS) of NaOsO<sub>3</sub> shown in the five investigated states (1) nonmagnetic without spin-orbit coupling (SOC); (2) nonmagnetic, including SOC; (3) G-type antiferromagnetic (AFM) with SOC and  $U = 0$ ; (4) G-type AFM with SOC and  $U = 1.0$  eV; and (5) G-type AFM with SOC and  $U = 2.0$  eV.

smaller than the crystal field splitting. In NaOsO<sub>3</sub>, with a formal  $t_{2g}^3 e_g^0$  configuration, the crystal field splitting separates the  $t_{2g}$  complex or  $\pi^*$  bands ( $\sim -2$  to  $2$  eV) from the  $e_g$  complex or  $\sigma^*$  bands ( $>2$  eV) leaving a gap of  $\sim 0.8$  eV between the top of the  $\pi^*$  band and the bottom of the  $\sigma^*$  band. The exchange energy further splits the  $\pi^*$  manifold into an occupied spin-up complex and an empty spin-down complex. The interatomic

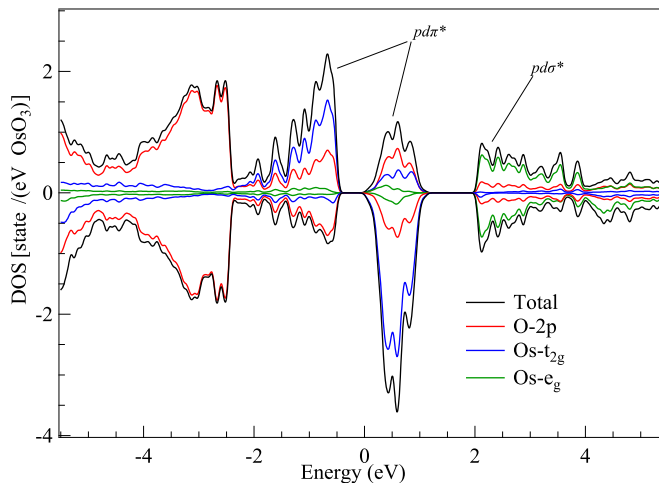


FIG. 7. The density of states (DOS) of a specific Os-centered octahedron OsO<sub>6/2</sub> (majority spin up) from the density functional theory (DFT) calculation with G-type antiferromagnetic (AFM) and  $U = 2.0$  eV without spin-orbit coupling (SOC). For this figure, the structure was rotated such that the Cartesian  $z$  axis aligned with the  $c$  axis of the system and the Cartesian  $x$  and  $y$  axes aligned with the bond configuration in the  $ab$  plane (a  $45^\circ$  rotation from the typical  $Pbnm$  structure) to allow a clean decomposition into  $t_{2g}$  and  $e_g$  manifolds. An adjacent octahedron would have identical DOS with up and down reversed.

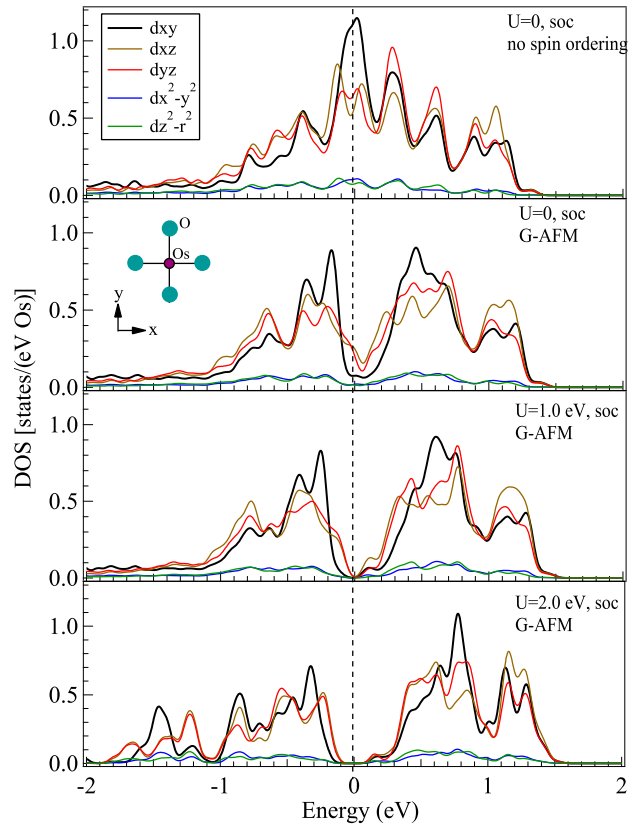


FIG. 8. The density of states (DOS) projected on the  $d$  orbitals for the five different electronic states simulated in NaOsO<sub>3</sub>. For simplicity of comparison with and without spin-orbit coupling, the DOS whether up or down (no spin-orbit coupling) or in the various  $j$  ( $= 1 + s$ ; spin-orbit coupled) quantum states have been added together and plotted on the positive  $y$  axis. The Cartesian  $x$  and  $y$  axes are the same as that in Fig. 7 and illustrated in an insert plot.

interaction causes a spin mixture in the exchange-split occupied and empty complexes separated at  $E_F$  by the exchange energy and  $U$ . As shown in Fig. 7, the occupied band includes mostly spin-up states and a significant portion of spin-down states for the  $t_{2g}$  originated complex. The  $p$ - $d$  hybridization is manifested by (1) a significant contribution of O-2p to the  $\pi^*$  band and (2) a nearly identical profile of  $N(E)$  for the  $t_{2g}$  and O-2p complex. However, the O-2p electrons are not spin polarized. The overlap of two spin bands and the  $d$ - $p$  hybridization results in a reduced (from the formal  $3 \mu_B$ ) moment of  $\mu \approx 1 \mu_B$  on Os<sup>5+</sup> from the self-consistent calculation, in good agreement with experiment.

As illustrated in Fig. 5, the orbital occupation of the  $xy$  orbital has a strong influence on the bond angle  $\alpha$ . Figure 8 displays the projected DOS of the three different orbitals of the  $t_{2g}$  complex. They all share a similar profile without spin polarization, indicating approximately equal occupation. The G-type AFM ordering splits the complex and places  $E_F$  at the minimum of the total DOS, but the  $xy$  band now contributes the least to states at  $E_F$ , and the bandwidth becomes the narrowest among three  $t_{2g}$  orbitals. These changes indicate that spin ordering and the easy axis due to the SOC (will be elaborated more below) allocates more electrons to the  $xy$

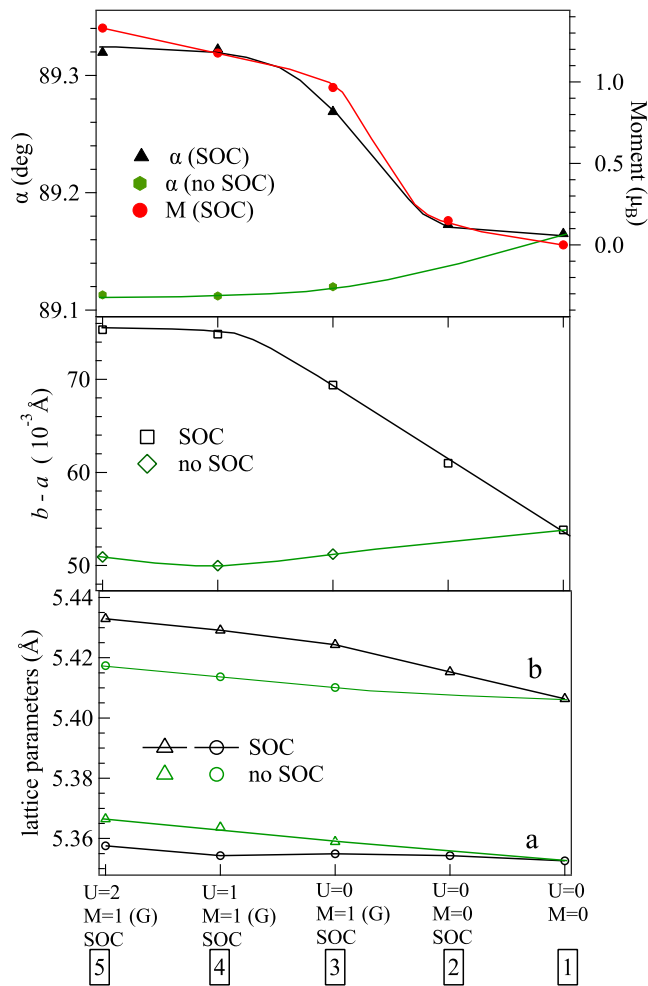


FIG. 9. The structural parameters in the relaxed structures for different electronic states as labeled in the figure. The electronic states correspond to the density of states (DOS) in Fig. 6. Lines in the plots are guides to the eye.

orbital than to the other two bands and that the  $xy$  orbital has the largest share of the total moment. Further increasing  $U$  opens a full gap,  $\Delta = E_{\text{ex}} + U$ , where  $E_{\text{ex}}$  is the exchange energy, which separates the majority up-spin band and majority down-spin band. The magnetic moment increases slightly along with the gap opening.

The calculated structural changes along with the evolution of the electronic states from State 1 ( $U = 0$ , nonmagnetic, no SOC) to State 5 ( $U = 2$ , G-type AFM, applied SOC) are summarized in Fig. 9. An increase in  $\alpha$  progressing from State 1 to State 5 matches essentially that shown in Fig. 4(b) derived from the crystallographic model based on experimental data, and the absolute value of the calculated  $\alpha$  is within  $0.1^\circ$  from the experimental result. This remarkably good agreement between simulation and experiment gives us confidence that we are capturing something important about the relevant physics, and we proceed to analyze the electronic ramifications of these structural changes. It is interesting to note that the moment in these relaxed structures tracks closely the change of  $\alpha$  through each of the five different states, which is consistent with the

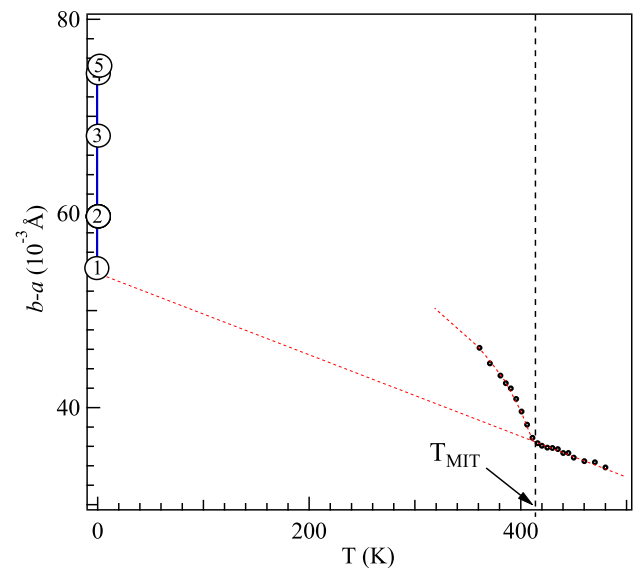


FIG. 10. The temperature dependence of lattice parameters from experiment and the simulation results in this paper.

argument that restoring  $\alpha$  toward  $90^\circ$  is a consequence of the orbital occupation.

Before our in-depth examination of the structural and electronic changes across  $T_{\text{MIT}}$ , we revisit the main relevant facts. The experiment shows that the  $b$  axis suddenly increases, while the  $a$  axis decreases across the transition. Together, these two changes cause no overall distinct change in the volume, although of course the volume is continuously decreasing with temperature due to thermal contraction. We will argue that the sudden changes are the consequence of localization that sets in at  $T_{\text{MIT}}$ , triggering a change in the bond angle  $\alpha$ . It is worth noting at this point that we force localization by manipulating  $U$  in our calculations but that there is no temperature since DFT is a ground state  $T = 0$  methodology. Therefore, the standard thermal contraction that has been seen in the data with decreasing temperature (and presumed increasing localization) will be missing from our results which are presented as increasing localization divorced from temperature.

Our calculations show that the  $b$  axis increases, whereas the  $a$  axis remains unchanged on crossing from State 1 to State 5 in Fig. 9. The overall change of  $b-a$  on crossing these electronic states matches very well with experimental data shown in Fig. 3(a). To account for the absence of thermal effects as described above, we fit the temperature dependence of  $b-a$  in the phase above  $T_{\text{MIT}}$  to a line in Fig. 10. The negative slope of the temperature dependence of  $b-a$  in  $\text{NaOsO}_3$  quantitatively matches that in  $\text{PrNiO}_3$  and  $\text{PrGaO}_3$  discussed above. The low-temperature extrapolation of the line to 0 K hits the location of  $b-a$  for State 1 surprisingly well. However, it is a long shot to predict the value of  $b-a$  at 0 K based on the curve of  $b-a$  within a narrow temperature range for the phase below  $T_{\text{MIT}}$ . Nevertheless, as shown in Fig. 10, all our reasonable guesses show it falling into a location covered by the five electronic states in the simulation. Therefore, the simulation of the five electronic states catches the essential structural changes on

crossing the MIT in  $\text{NaOsO}_3$ . Our calculations show that the  $a$ -axis value is essentially flat (although it reduces slightly from State 3 to State 4 in the low panel of Fig. 9) across the different states of localization, as is observed in experiment on cooling through the metal insulator transition. However, the difference is small and is compensated by the overestimation of the increase in the  $b$  lattice parameter which brings  $b$ - $a$  into good agreement with observation. The likely source of this systematic error is the known overestimation of lattice parameters in the GGA which both exaggerates the  $b$  increase and suppresses the  $a$  decrease.

It is important to note that the monotonic increase of  $\alpha$  along the evolution from itinerant to localized electronic behavior is not simply driven by minimizing the Coulomb energy while the  $xy$  orbital is increasingly occupied, as indicated by the Madelung energy calculation or even by factoring in  $p$ - $d$  directional hybridization. The SOC also plays a critical role. In our relaxed calculations, the easy axis is found to be along the  $a$  axis, as is the experimental case without exception in G-type AFM  $Pbnm$  perovskites. Attempts to establish a different direction computationally were unsuccessful if the structure was allowed to relax. The trend of  $\alpha$  is opposite if SOC is not included in the calculation, as is shown in the upper panel of Fig. 9, underlining the importance of the SOC as a partial determining factor in the localization across the transition.

## VI. DISCUSSION

### A. Electronic behavior revealed by the paramagnetic magnetic susceptibility

Itinerant electrons in the Fermi sea become polarized under a magnetic field for a small portion of the DOS in the energy range of  $kT$  near the Fermi energy. The first term of thermodynamic expression of magnetic susceptibility for itinerant electrons gives a  $\chi(T) \sim \mu_B^2 N(E_F)$ , known as the Pauli formula [31]. In the extreme limit of localized electrons, i.e., isolated magnetic ions of in the gas phase, the magnetic moment is independent of temperature, which leads to the Curie law  $\chi(T) = C/T$ , where  $C$  is the Curie constant and can be related to the effective moment  $\mu_{\text{eff}}$ . In a solid, exchange interactions lead to long-range magnetic orderings, and the Curie law is reformulated as the Curie-Weiss (C-W) law  $\chi = C/(T - \Theta)$ , where the Weiss constant can be related to the ordering temperature  $|\Theta| \sim T_N$  or  $T_c$ . The C-W law is valid only if fitting  $\chi(T)$  to the formula of the C-W law gives a reasonable value of  $|\Theta|$ . Electron-electron correlations in metals such as  $\text{LaCuO}_3$  and  $\text{LaNiO}_3$  contribute a weak temperature dependence to the paramagnetic susceptibility [32]. Their inverse susceptibility, especially at high temperatures, can be closely fit to a line, but this fitting yields a huge  $|\Theta|$  and  $\mu_{\text{eff}}$  in these paramagnetic metals. This kind of metal was studied in the 1970s and generally described as an enhanced Pauli paramagnetism [33,34]. For itinerant electron systems with magnetic ordering, such as  $\text{ZrZn}_2$  [35], the new C-W law proposed by Moriya [36] should be applied. The Curie constant, which is not relevant to  $\mu_{\text{eff}}$  in this law, is inversely proportional to  $N(E_F)$ .

As mentioned in the introduction, fitting  $\chi(T)$  in the paramagnetic phase of  $\text{NaOsO}_3$  to a C-W law gives a

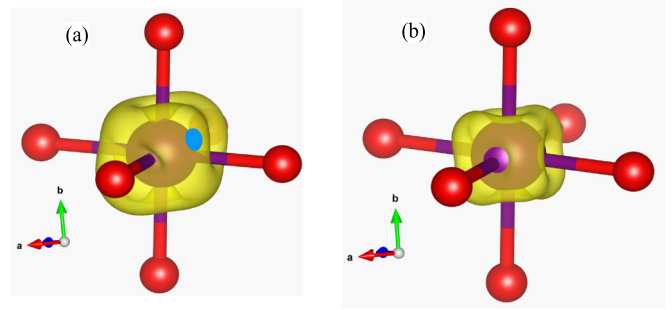


FIG. 11. The isosurface (level = 0.0043) of charge density distribution in an  $\text{OsO}_6$  octahedron, (a)  $U = 0$  eV, spin-orbit coupling (SOC), and  $M = 0$ ; (b)  $U = 2.0$  eV, SOC, and  $M = 1$ .

$|\Theta| = 1949$  K  $\gg T_N = T_{\text{MIT}} = 410$  K. This observation well qualifies the phase of  $\text{NaOsO}_3$  above  $T_{\text{MIT}}$  as a correlation-enhanced Pauli metal like  $\text{LaNiO}_3$  and  $\text{LaCuO}_3$  and reasonably assigned as State 1 (no SOC) or State 2 (SOC) in our DFT calculation. The SOC effect on the paramagnetic susceptibility is to introduce the nonlinear behavior in the plot of inverse  $c$  vs temperature [37,38], for example, in 9R  $\text{BaRuO}_3$  [39]. The linear  $\chi^{-1}(T)$  indicates a much weaker SOC effect in the paramagnetic state of  $\text{NaOsO}_3$ . Therefore, we could attribute the paramagnetic phase to State 1. As detailed earlier, the overall change of  $\alpha$  calculated for increasing localization as simulated by the electronic states from State 1 to State 5 matches that derived from the measured lattice parameters on crossing  $T_{\text{MIT}}$ . The overall change of magnetic moment from 0 to  $\sim 1 \mu_B$  along with the increase of  $\alpha$  is consistent with the electron localization and increased orbital occupation from the enhanced Pauli metal phase on cooling through  $T_{\text{MIT}}$ .

### B. The preferred local structure in the systems with no orbital degeneracy

The cooperative JT effect [40] is a structural instability connected to the lifting of an orbital degeneracy by the structural distortions in general and lowering the global symmetry in some cases. The JT effect is also accompanied by a dramatic change of physical properties such as a conductor-to-insulator transition in  $\text{LaMnO}_3$  with the  $t_{2g}^3 e_g^1$  configuration [41].  $\text{NaOsO}_3$  has a  $t_{2g}^3 e_g^0$  configuration and adopts the orthorhombic perovskite structure, having the intrinsic structural distortion exemplified by  $\text{LaGaO}_3$  [42], a perovskite that has no orbital degeneracy or spin ordering, and an  $\alpha < 90^\circ$ . Our DFT calculations show an electron density in the nonmagnetic metallic phase of  $\text{NaOsO}_3$  (resembling the phase at  $T > T_{\text{MIT}}$ ) as viewed by the isosurface plot around Os in an  $\text{OsO}_6$  octahedron in Fig. 11(a). Whereas the isosurface still keeps the essential features of the electron distribution in the  $\pi^*$  band, the distortions of the isosurface reflect the strong hybridization between the  $d$  and  $p$  orbitals in the oxide. The insulator phase with  $U = 2.0$  eV has an isosurface of electron density that has a more regular shape for the typical occupation of three  $t_{2g}$  orbitals. In addition, more charge density is moved away from the Os-O bonding directions to the area of  $xy$ ,  $xz$ , and  $yz$  orbitals. The change of charge density from the metallic phase to the insulator phase imposes a structural

preference, i.e., an O-Os-O bond angle closing to  $90^\circ$  in an octahedron, as demonstrated by the point charge model in Fig. 5. The structural preference due to the change of electronic state competes with the intrinsic structural distortion at  $T_{\text{MIT}}$  in  $\text{NaOsO}_3$ .

### C. Mott transition vs Slater transition

In his book [43], Mott classified the Slater transition as an itinerant band analog to a strong correlation-driven MIT. In the picture of a Slater transition, electrons remain itinerant crossing the transition. The gap is opened at  $E_F$  which intercepts with the reduced Brillouin boundary due to a symmetry change associated with the AFM ordering. While it does split the majority-spin occupied and the minority-spin empty bands, the AFM ordering alone does not open up a clean gap at  $E_F$  in  $\text{NaOsO}_3$ , as indicated from the DFT calculation, shown as State 3 in Fig. 6. We call the MIT at  $T_{\text{MIT}}$  a muted Mott transition because of no obvious change in the cell volume at the transition. However, all other features of Mott physics stay, such as the occupation of atomic orbitals at  $T < T_{\text{MIT}}$  and the correlation fluctuations at  $T > T_{\text{MIT}}$ . Clear evidence of the correlation fluctuations has been demonstrated in a RIXS experiment [8,9]. The structural study and the DFT calculations presented in this paper show clear evidence of orbital occupation at  $T < T_{\text{MIT}}$ . It must be stressed that SOC also plays an important role in facilitating the muted Mott transition in  $\text{NaOsO}_3$ . The opening of a gap at the Fermi energy is not as simple as increasing  $U$  to a critical value as other DFT calculations in the literature [10–12]. Opening a gap at  $U_c$  along with the particular structural change on crossing  $T_{\text{MIT}}$  in the orthorhombic  $\text{NaOsO}_3$  can be simulated only if SOC and the correct easy axis are incorporated in the calculation. The magnetocrystalline single-ion anisotropy (MSIA) originates from SOC. In the case of  $\text{NaOsO}_3$  (and in all orthorhombic Pbnm oxides with G-type AFM), MSIA places the easy axis of the moment along the  $a$  axis. The spin direction appears to facilitate an opening up of  $\alpha$  which is also required by the electron occupation on the  $xy$  orbital.

## VII. CONCLUSIONS

The MIT in the  $\text{NaOsO}_3$  perovskite is not associated with a discontinuous change of the cell volume or change in crystal symmetry but rather in a pronounced splitting of the lattice parameters  $a$  and  $b$  in the orthorhombic perovskite structure. There have been no attempts to elucidate the mechanism behind this change of lattice parameters or its effect on electronic structure. In this paper, we have correlated the change of lattice parameters with an octahedral-site distortion, parametrized by the bond angle  $\alpha$ , which is commonly seen in the orthorhombic perovskite oxides. We subsequently correlate the change in  $\alpha$  to changes in the electronic structure. This change has likely been previously missed due to its relative subtlety, but noting that  $\alpha$  changes only  $\sim 1^\circ$  from  $\text{LuFeO}_3$  all the way to  $\text{LaFeO}_3$ , the change we find  $\Delta\alpha \approx 0.15^\circ$  in a narrow temperature range around the MIT in  $\text{NaOsO}_3$  is dramatic. It reflects a structural change precipitated by the preference of localized electrons in conjunction with SOC, which competes with the intrinsic perovskite structural distortion. The discovery of this local structural change suggests the MIT found in the  $5d$  transition-metal oxide  $\text{NaOsO}_3$  cannot be fully attributed to the Slater mechanism; it should be treated as somewhat more closely associated with a Mott transition.

## ACKNOWLEDGMENTS

This paper was primarily financially supported by the National Science Foundation (NSF) through the Center for Dynamics and Control of Materials: an NSF Materials Research Science and Engineering Center under Cooperative Agreements No. DMR-1720595 and No. DMR-2132574 and the Office of Naval Research through the U.S. Naval Research Laboratory Basic Science Program and the Summer Research Faculty Program. J.S.Z. thanks S. Calder for providing the original cif files of the published neutron-diffraction data and Kevin May and Bongjae Kim for useful discussions.

- 
- [1] Y. G. Shi, Y. F. Guo, S. Yu, M. Arai, A. A. Belik, A. Sato, K. Yamaura, E. Takayama-Muromachi, H. F. Tian, H. X. Yang *et al.*, Continuous metal-insulator transition of the antiferromagnetic perovskite  $\text{NaOsO}_3$ , *Phys. Rev. B* **80**, 161104(R) (2009).
- [2] S. Calder, V. O. Garlea, D. F. McMorrow, M. D. Lumsden, M. B. Stone, J. C. Lang, J. W. Kim, J. A. Schlueter, Y. G. Shi, K. Yamaura *et al.*, Magnetically driven metal-insulator transition in  $\text{NaOsO}_3$ , *Phys. Rev. Lett.* **108**, 257209 (2012).
- [3] J. S. Zhou, L.-P. Cao, J. A. Alonso, J. Sanchez-Benitez, M. T. Fernandez-Diaz, X. Li, J.-G. Cheng, L. G. Marshall, C. Q. Jin, and J. B. Goodenough, Possible Bose-Einstein condensate associated with an orbital degree of freedom in the Mott insulator  $\text{CaCrO}_3$ , *Phys. Rev. B* **94**, 155137 (2016).
- [4] T. Moriya, Anisotropic superexchange interaction and weak ferromagnetism, *Phys. Rev.* **120**, 91 (1960).
- [5] N. Gurung, N. Leo, S. P. Collins, G. Nisbet, G. Smolentsev, M. Garcia-Fernandez, K. Yamaura, L. J. Heyderman, U. Staub, Y. Joly *et al.*, Direct observation of electron density reconstruction at the metal-insulator transition in  $\text{NaOsO}_3$ , *Phys. Rev. B* **98**, 115116 (2018).
- [6] J. C. Slater, Magnetic effects and the Hartree-Fock equation, *Phys. Rev.* **82**, 538 (1951).
- [7] I. Lo Vecchio, A. Perucchi, P. Di Pietro, O. Limaj, U. Schade, Y. Sun, M. Arai, K. Yamaura, and S. Lupi, Infrared evidence of a Slater metal-insulator transition in  $\text{NaOsO}_3$ , *Sci. Rep.* **3**, 2990 (2013).
- [8] J. G. Vale, S. Calder, C. Donnerer, D. Pincini, Y. G. Shi, Y. Tsujimoto, K. Yamaura, M. M. Sala, J. van den Brink, A. D. Christianson *et al.*, Evolution of the magnetic excitations in  $\text{NaOsO}_3$  through its metal-insulator transition, *Phys. Rev. Lett.* **120**, 227203 (2018).

- [9] J. G. Vale, S. Calder, C. Donnerer, D. Pincini, Y. G. Shi, Y. Tsujimoto, K. Yamaura, M. M. Sala, J. van den Brink, A. D. Christianson *et al.*, Crossover from itinerant to localized magnetic excitations through the metal-insulator transition in  $\text{NaOsO}_3$ , *Phys. Rev. B* **97**, 184429 (2018).
- [10] Y. P. Du, X. G. Wan, L. Sheng, J. M. Dong, and S. Y. Savrasov, Electronic structure and magnetic properties of  $\text{NaOsO}_3$ , *Phys. Rev. B* **85**, 174424 (2012).
- [11] B. Kim, P. T. Liu, Z. Ergonen, A. Toschi, S. Khmelevskiy, and C. Franchini, Lifshitz transition driven by spin fluctuations and spin-orbit renormalization in  $\text{NaOsO}_3$ , *Phys. Rev. B* **94**, 241113(R) (2016).
- [12] M. C. Jung, Y. J. Song, K. W. Lee, and W. E. Pickett, Structural and correlation effects in the itinerant insulating antiferromagnetic perovskite  $\text{NaOsO}_3$ , *Phys. Rev. B* **87**, 115119 (2013).
- [13] S. Middey, S. Debnath, P. Mahadevan, and D. D. Sarma,  $\text{NaOsO}_3$ : A high Neel temperature  $5d$  oxide, *Phys. Rev. B* **89**, 134416 (2014).
- [14] J. S. Zhou and J. B. Goodenough, Unusual evolution of the magnetic interactions versus structural distortions in  $\text{RMnO}_3$  perovskites, *Phys. Rev. Lett.* **96**, 247202 (2006).
- [15] G. G. Guzman-Verri, R. T. Brierley, and P. B. Littlewood, Cooperative elastic fluctuations provide tuning of the metal-insulator transition, *Nature (London)* **576**, 429 (2019).
- [16] M. Imada, A. Fujimori, and Y. Tokura, Metal-insulator transitions, *Rev. Mod. Phys.* **70**, 1039 (1998).
- [17] J. B. Torrance, P. Lacorre, A. I. Nazzari, E. J. Ansaldo, and C. Niedermayer, Systematic study of insulator-metal transitions in perovskites  $\text{RNiO}_3$  ( $R = \text{Pr, Nd, Sm, Eu}$ ) due to closing of charge-transfer gap, *Phys. Rev. B* **45**, 8209 (1992).
- [18] J. S. Zhou, J. B. Goodenough, B. Dabrowski, P. W. Klamut, and Z. Bukowski, Enhanced susceptibility in  $\text{LNiO}_3$  perovskites ( $L = \text{La, Pr, Nd, Nd}_{0.5}\text{Sm}_{0.5}$ ), *Phys. Rev. Lett.* **84**, 526 (2000).
- [19] J. S. Zhou, J. B. Goodenough, and B. Dabrowski, Exchange interaction in the insulating phase of  $\text{RNiO}_3$ , *Phys. Rev. Lett.* **95**, 127204 (2005).
- [20] M. O’Keeffe and B. G. Hyde, Some structures topologically related to cubic perovskite ( $E2_1$ ),  $\text{ReO}_3$  ( $D0_9$ ) and  $\text{Cu}_3\text{Au}$  ( $L1_2$ ), *Acta Cryst. B* **33**, 3802 (1977).
- [21] M. W. Lufaso and P. M. Woodward, Prediction of the crystal structures of perovskites using the software program SPuDS, *Acta Cryst. B* **57**, 725 (2001).
- [22] J. S. Zhou and J. B. Goodenough, Universal octahedral-site distortion in orthorhombic perovskite oxides, *Phys. Rev. Lett.* **94**, 065501 (2005).
- [23] P. M. Woodward, T. Vogt, D. E. Cox, A. Arulraj, C. N. R. Rao, P. Karen, and A. K. Cheetham, Influence of cation size on the structural features of  $\text{Lu}_{1/2}\text{A}_{1/2}\text{MuO}_3$  perovskites at room temperature, *Chem. Mater.* **10**, 3652 (1998).
- [24] L. Vasylechko, Ye Pivak, A. Senyshyn, D. Savytskii, M. Berkowski, H. Borrmann, M. Knapp, and C. Paulmann, Crystal structure and thermal expansion of  $\text{PrGaO}_3$  in the temperature range 12–1253 K, *J. Solid State Chem.* **178**, 270 (2005).
- [25] T. C. Huang, W. Parrish, H. Toraya, P. Lacorre, and J. B. Torrance, High-temperature crystal structures of orthorhombic and rhombohedral  $\text{PrNiO}_3$ , *Mater. Res. Bull.* **25**, 1091 (1990).
- [26] J. S. Zhou and J. B. Goodenough, Local structural distortions, orbital ordering, and ferromagnetism in underdoped  $\text{La}_{1-x}\text{Sr}_x\text{MnO}_3$ , *Phys. Rev. B* **91**, 064414 (2015).
- [27] G. Kresse and J. Hafner, *Ab initio* molecular dynamics for liquid metals, *Phys. Rev. B* **47**, 558 (1993).
- [28] P. E. Blöchl, Projector augmented-wave method, *Phys. Rev. B* **50**, 17953 (1994).
- [29] J. P. Perdew, K. Burke, and M. Ernzerhof, Generalized gradient approximation made simple, *Phys. Rev. Lett.* **77**, 3865 (1996).
- [30] S. L. Dudarev, G. A. Botton, S. Y. Savrasov, C. J. Humphreys, and A. P. Sutton, Electron-energy-loss spectra and the structural stability of nickel oxide: An LSDA+U study, *Phys. Rev. B* **57**, 1505 (1998).
- [31] C. Kittel, *Introduction to Solid State Physics*, 7th ed. (John Wiley and Sons, Singapore, 1996).
- [32] J. S. Zhou, L. G. Marshall, and J. B. Goodenough, Mass enhancement versus Stoner enhancement in strongly correlated metallic perovskites:  $\text{LaNiO}_3$  and  $\text{LaCuO}_3$ , *Phys. Rev. B* **89**, 245138 (2014).
- [33] G. Demazeau, A. Marbeuf, M. Pouchard, and P. Hagenmuller, Sur une serie de composés oxygènes du nickel trivalent dérivés de la perovskite, *J. Solid State Chem.* **3**, 582 (1971).
- [34] J. B. Goodenough, N. F. Mott, M. Pouchard, and G. Demazeau, Etude comparative du comportement magnétique des phases  $\text{LaNiO}_3$  et  $\text{LaCuO}_3$ , *Mat. Res. Bull.* **8**, 647 (1973).
- [35] S. Ogawa and N. Sakamoto, Magnetic properties of  $\text{ZrZn}_2$ —Itinerant electron ferromagnet, *J. Phys. Soc. Jpn.* **22**, 1214 (1967).
- [36] T. Moriya, *Electron Correlation and Magnetism in Narrow-Band Systems* (Springer-Verlag, Berlin, 1981).
- [37] J. Kanamori, Theory of the magnetic properties of ferrous and cobaltous oxides, I, *Prog. Theor. Phys.* **17**, 177 (1957).
- [38] J. Kanamori, Theory of the magnetic properties of ferrous and cobaltous oxides, II, *Prog. Theor. Phys.* **17**, 197 (1957).
- [39] M. Drillon, L. Padel, and J.-C. Bernier, Effects of spin-orbit coupling and exchange in  $\text{BaRuO}_3$ , *J. Chem. Soc. Faraday Trans. 2* **75**, 1193 (1979).
- [40] J. B. Goodenough, *Magnetism and the Chemical Bond* (John Wiley and Sons, New York, 1963).
- [41] J. S. Zhou and J. B. Goodenough, Paramagnetic phase in single-crystal  $\text{LaMnO}_3$ , *Phys. Rev. B* **60**, R15002 (1999).
- [42] M. Berkowski, J. Fink-Finowicki, P. Byszewski, R. Diduszko, E. Kowalska, R. Aleksyko, W. Piekarczyk, L. O. Vasylechko, D. I. Savytskij, L. Perchuc *et al.*, Growth and structural investigations of  $\text{La}_{1-x}\text{Pr}_x\text{GaO}_3$  solid solution single crystals, *J. Cryst. Growth* **222**, 194 (2001).
- [43] N. F. Mott, *Metal-Insulator Transitions* (Yaylor and Francis, London, 1990).